Direct Analysis of Stacked Au/Ti/In_2O_3/Al_2O_3/p^+-Si Transport Mechanisms Using *operando* Hard X-ray Photoelectron Spectroscopy

Ibrahima Gueye*,[1,2] Shigenori Ueda,[1,3,4] Atsushi Ogura,[5,6] and Takahiro Nagata*[1,6]

[1]*Research Center for Functional Materials, National Institute for Materials Science (NIMS), 1-1 Namiki, Tsukuba, Ibaraki 305-0044, Japan*
[2]*Center for Synchrotron Radiation Research, Japan Synchrotron Radiation Research Institute (JASRI), 1-1-1 Kouto, Sayo, Hyogo 679-5198, Japan.*
[3]*Research Center for Advanced Measurement and Characterization, NIMS,1-2-1 Sengen, Tsukuba, Ibaraki 305-0047, Japan*
[4]*Synchrotron X-ray Station at SPring-8, NIMS, 1-1-1 Sayo, Hyogo 379-5148, Japan*
[5]*Meiji Renewable Energy Laboratory, Meiji University, 1-1-1 Higashimita, Tama-ku, Kawasaki, Kanagawa 214-8571, Japan.*
[6]*Graduate School of Science and Technology, Meiji University, 1-1-1 Higashimita, Tama-ku, Kawasaki, Kanagawa 214-8571, Japan.*
Corresponding Authors: ibrahima.gueye@spring8.or.jp; NAGATA.Takahiro@nims.go.jp

ABSTRACT: Oxygen transport mechanisms for two different Au/Ti/In_2O_3/Al_2O_3/p^+-Si samples were experimentally evaluated with hard X-ray photoelectron spectroscopy (HAXPES). The deposition temperature for atomic layer deposition (ALD) of In_2O_3, as well as the bias voltages applied on the entire stacked structures, were the main parameters used in the work. Chemical analyses of the In_2O_3 layers deposited at 150 °C and 200 °C for the samples named T_150 and T_200, respectively, revealed a decreased carbon impurity content in the host In_2O_3 used as a dopant. *Ex-situ* interfacial analysis of In_2O_3/Al_2O_3 also indicated oxygen transport from Al_2O_3 to In_2O_3. Moreover, we observed that the Ti adhesion metal attracted oxygen and carbon from the In_2O_3 to form TiO_2 and TiC conductive interlayers. Furthermore, *operando*-HAXPES under an applied bias voltage also revealed that In_2O_3 underwent phase separation, likely due to variations in the space charge (carriers) around the In_2O_3/Al_2O_3 interface for the T_150 sample. Finally, our results emphasize the prominent roles of migration for the ionic oxygen/carbon species and the uncompensated interfacial charge formed by the bias voltage for the metal-semiconductor-oxide stacked structure.

Keywords: *Operando*, HAXPES, Buried-interfaces, In_2O_3, Al_2O_3, Band bending, Chemical-structures

I. INTRODUCTION

Thin film transistors (TFTs) have undergone extensive evo-lution, development, and refinement[1,2]. Recently, amorphous oxide semiconductors (AOS) have been proposed as propi-tious alternatives to extend the limits of the amorphous sil-icon (a-Si) semiconductors predominantly used as channel layers in TFTs[3]. AOS materials involving cations with the $(n-1)d^{10}ns^0 (n \geq 4)$ electronic configuration provide perfor-mance enhancements thanks to their high conductivities, high transparencies, and excellent mechanical properties[4]. Indeed, charge carriers for AOS migrate through the TFTs at rates 20 to 40 times faster than those for a-Si TFTs. In addition, the ad-vantages of the AOS materials over the current a-Si technol-ogy include superior surface planarity and easy manufactur-ing on plastic substrates at low servicing temperatures, which leads to flexible electronics without compromising their ex-cellent properties[5].

From the perspective of TFT applications, the AOS chan-nel materials require reasonably low carrier densities and high electron mobilities while also providing good ohmic con-tact to source/drain electrode materials. Among a plethora of amorphous oxide semiconductors (AOS), indium ox-ide (In_2O_3) emerges as a compelling and promising can-didate for transparent and flexible electronics. Its ap-peal stems from its wide band gap, high carrier mobil-ity ($\sim$ 40 cm^2/Vs), and compatibility with diverse appli-cations necessitating transparency and low-temperature deposition[6–8]. However, it is notable that consensus re-garding the precise value of the In_2O_3 band gap remains elusive[9–12]. It is imperative to acknowledge that band gap values can exhibit variability within a defined range ow-ing to factors such as experimental techniques, sample preparation methods, measurement conditions, or theo-retical calculations. In 2013, Irmscher et al.[11] conducted optical absorption measurements on In_2O_3 single crystals with very low defect density, reporting an optically mea-sured gap of approximately 2.7 eV, consistent with the elec-tronic or fundamental gap. Conversely, Muydinov et al.[12] posited that pure In_2O_3 cannot possess an indirect gap due to the parabolic nature of the conduction band. Addition-ally, they asserted that the minimum electronic or funda-mental band gap, symmetrically forbidden, hovers around 2.9 eV, with the first allowed transition originating from a level roughly 0.8 eV below the valence band top, yielding the commonly observed optical band gap value of approx-imately 3.7 eV. These recent findings align with previous calculations by Karazhanov et al.[10].

In_2O_3 unfortunately exhibits instability over time, pos-ing a significant hurdle to its future commercialization. This instability is largely attributed to the presence of an uncontrollable excess of oxygen vacancies (V_O^{2+})[13]. In-deed, oxygen migration outwards from amorphous In_2O_3 at room temperature under air or vacuum conditions due to the relatively low dissociation energy of the In-O bond has been previously reported[14,15]. Fuh et al.[14] observed a decrease in threshold voltage (V_{th}) values of amorphous IGZO-TFTs with prolonged exposure to the environment,

where the average threshold voltage shifted from 10.2 V to 5.8 V after a 9-day duration. They linked the insta-bility of passivation-free amorphous IGZO-TFT channels to the exposure of the a-IGZO layer to ambient condi-tions. The authors suggested that the weak bond of oxy-gen atoms (BDE: 346 kJ/mol[16]) lacked sufficient energy for structural relaxation during annealing, leading to easy desorption of oxygen atoms from the a-IGZO film and the formation of oxygen vacancies, thereby providing free car-riers. The precise mechanism (vacancy-mediated diffu-sion, interstitial diffusion, grain boundary diffusion, sur-face diffusion, etc.) by which oxygen is transported out of the amorphous In_2O_3 thin film remains unclear to date. In addition, the degree of similarity between the structure and properties of point defects in amorphous solids and those in the crystalline phase remains a subject of ongoing debate and exceeds the scope of this report[17,18]. However, the presence of excess V_O^{2+} defects, each offering two elec-trons, inevitably leads to a transition from semiconduct-ing to metallic behavior[19–21]. Additionally, the V_O^{2+} sites in the TFTs have been identified as the cause of negative V_{th} shifts in the transfer characteristics[22,23]. These sites are also suspected of influencing other TFT properties, in-cluding carrier concentration/mobility, current on/off ra-tio, subthreshold swing, and contact resistance. To mit-igate the issues associated with V_O^{2+} defects, numerous research groups have pursued various optimization strate-gies.

Simple chemical doping process represents one of the most common methods to regulate the excess carrier of In_2O_3 with precise control over the doping process. Adding elements such as Ti[8,16], W[8,16], La[24], Ga[25], and Si[8] are also expected to stabilize the existing V_O^{2+}. In addition, the defect stabi-lization process will cancel the out-diffusion of the oxygen atoms from the In_2O_3 matrix by raising the In-O BDE.

Furthermore, a doping process by controlling the deposi-tion temperature has been lately reported as a practical way of improving In_2O_3 electrical performance and stability. In this later method, the variation of the deposition temperature can affect the decomposition and reaction of precursors and lead to changes in the film's properties, including its conduc-tivity, bandgap, or structural characteristics. More recently, it has been reported that low-temperature deposited In_2O_3 films grown by an atomic layer deposition (ALD) method showed the presence of impurities, which mainly consisted of carbon[26]. This residual carbon was expected to mitigate the V_O^{2+} issues specially observed at 200 ˚C deposition tem-peratures. Indeed, from these papers[26], authors claim that the involvement of these carbon impurities at 150 ˚C reduces the V_O^{2+} and allows transistor to reach a threshold voltage (V_{th}) of 3.2 V and high mobility of 20.4 cm^2/Vs. Finally, from the transfer and output characteristics of the In_2O_3-based TFT, au-thors also reported a large negative V_{th} shift with higher de-position temperature while no V_{th} shift was observed at lower deposition temperature.

Post-thermal annealing (PTA) under an oxygen atmosphere has been also used to partially compensate for the oxygen losses from In_2O_3[13,27]. Ma and coworkers also reported the positive influence of the PTA process on In_2O_3-TFTs[28], which was also suggested earlier by Yeom *et al.*[29]. Note that post-process annealing has been also shown to improve the thresh-old voltage shift[30], field-effect mobility[31,32] and channel-to-source/drain metallization interface resistivity[33–35].

The effects of these aforementioned In_2O_3 thermal treat-ments on the chemical and electronic structures of the adjacent layers and buried interfaces must also be considered seriously during optimization of the indium oxide-based TFTs[36–38]. Generally, the subthreshold swings (SS: the minimum gate voltage required to switch the transistor from OFF to ON) or V_{th} of AOS-TFT devices are mainly determined by the qual-ity of the AOS-gate dielectric interface. As we expected, the thermal conditions used for TFT manufacturing will affect the AOS-gate dielectric interface.

To make excellent ohmic contact at the AOS-source (AOS-drain) heterojunction, it is important to select metal electrodes with low specific resistivities. Indeed, high specfic contact resistance at the AOS-source (or drain) metallization interface is associated with decreases in the field effect mobility. The chemical states at the interfaces and the effects of common metal contacts on TFT stability should be also considered to improve the TFT performance.

Therefore, it seems necessary to shed more light on the changes in the chemical structures occurring in the films and buried interfaces TFT devices with non-destructive analyses. Hard X-ray photoelectron spectroscopy (HAXPES)[39–41] is a suitable method to study the chemical states of buried layers and interfaces in real device structures with a non-destructive way owing to a large probing depth of photoelectrons with several ten nanometers. Thus, with HAXPES analyses for In_2O_3-based TFTs, we will be able (1) to observe how oxy-gen species move and react inside stacked devices, (2) to see whether C doping has the expected effect on In_2O_3 such as a reduction in the V_O^{2+} level as well as suppression of vacancy migration, and (3) to confirm whether there are further issues that must be addressed to improve the general performance of the device.

Since the purpose of this work is limited to understand-ing the reactions (mainly oxygen) that occur as a result of the deposition as well as PTA temperatures and the applied external electric field, we only focus on the prototypical Au/Ti/In_2O_3/Al_2O_3/p^+-Si stacked structure and not on a full TFT device.

II. EXPERIMENTAL SECTION

A. Materials and Preparation

Amorphous In_2O_3 films were grown on Al_2O_3/p^+-Si sub-strates by using an AT-400 ALD System from Anric Tech-nologies. For low-temperature In_2O_3 deposition using met-alorganic precursors, a liquid ethylcyclopentadienyl indium (InEtCp) compound was used[42]. In reference to the In_2O_3 deposition temperature, the In_2O_3/Al_2O_3/p^+-Si samples with In_2O_3 deposition at 150 °C and 200 °C were labelled T_150-bare and T_200-bare, respectively, as shown in Figure 1(a).

The fully stacked Au/Ti/In_2O_3/Al_2O_3/p^+-Si samples with Au/Ti top electrodes were named T_150 and T_200, respectively, as depicted in Figure 1(b).

For each sample, a 5-nm-thick In_2O_3 layer on a 5-nm-thick Al_2O_3 layer was deposited on a heavily doped p^+-Si substrate (bottom electrode), as follows. First, the p^+-Si substrate was cleaned with an organic solvent solution and deionized water, followed by cleaning with HF solution to remove a native SiO_2 layer. Then, a trimethylaluminium ($(CH_3)_3Al$) precur-sor and O_3 oxidant gas were used to deposit the amorphous Al_2O_3 layer via ALD at 200 °C. The presence of unintention-ally formed SiO_2 intermediate layer between the p^+-Si and Al_2O_3 layers was already identified and reported in our previ-ous work[43].

Then, In_2O_3 layers were grown on the Al_2O_3 layer by ALD. The ALD process consisted of alternating exposure to the In-EtCp precursor and the H_2O/O_3 oxidant gases, as follows[13]. The temperature of the InEtCp precursor was fixed at 80 °C, and N_2 was used as both the carrier and purge gas. Then, to improve the properties of the indium oxide, PTA was performed on the T_150-bare and T_200-bare samples for 90 min at 150 °C under an O_3 atmosphere. Finally, to evaluate the de-vice properties under the bias voltages, Au/Ti were patterned on the T_150-bare and T_200-bare layers by electron beam evaporation to obtain T_150 and T_200 (Figure 1). The sur-face size associated with the top electrode stacked device was 3 mm × 2 mm.

B. Stacked device characterization

The HAXPES measurements at room temperature and with a stable base pressure ($\sim 10^{-7}$ Pa) were conducted at BL15XU at the SPring-8 synchrotron radiation facility in Japan[44]. Since the angle between the incoming X-ray and the photoelectron analyzer was set to 90^o, the X-ray beam impinged on samples with a grazing angle of 5^o in our experimental setup (Figure 1). This experimental geometry with a take-off angle (TOA: the angle between the sample surface and photoelectrons entering the analyzer) of 85^o was chosen to increase as much as possible the probing depth through the stacked devices. With this TOA of 85^o, an X-ray beam with an expanded footprint size of approximately 400 × 30 $\mu\ m^2$ was projected on the surfaces. The excitation photon energy was set to 5.95 keV, and photoelectrons were analyzed with a hemispherical electron analyzer (VG-Scienta R4000). The total energy resolution was 0.24 eV determined by fitting the Au Fermi edge. The binding energy (BE) was calibrated by using the Fermi edge of Au.

The inelastic mean free paths (IMFPs) of photoelectrons were calculated with QUASES-TPP2M software, and probing depth d is ∼3 times the IMFPs[45]. With binding energy of 99.3 eV for Si $2p_{3/2}$, 1561.8 eV for Al 1s and 445.4 eV for In $3d_{5/2}$ at the excitation photon energy of 5.95 keV, we estimated d as approximately 30.4 nm, 24.6 nm, and 21.0 nm, respectively, for a TOA of 85^o. These latter d values were multiplied by factors of 0.77, 0.5, and 0.17 when the TOAs were fixed at 50^o, 30^o and 10^o, respectively, according to the equation $d \sim 3 \times IMFP \times sin(TOA)$.

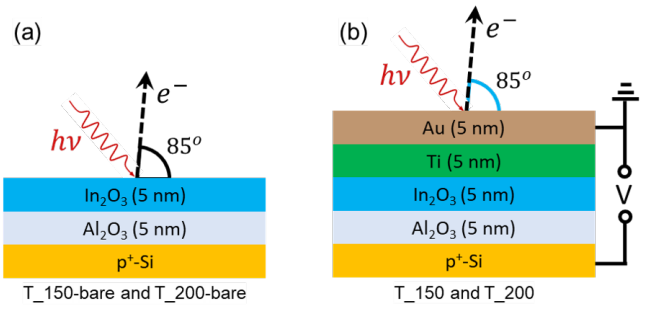

FIG. 1: Schematic illustration of (a) T_150-bare and T_200-bare samples for HAXPES measurements and (b) T_150 and T_200 samples for *operando*-HAXPES.

For the *operando* analysis, an ADCMT 6241A DC Volt-age current source/monitor system interfaced with an external PC controller was used to apply different bias voltages to the samples, as depicted in Figure 1(b) during the HAXPES measurements. The duration of each measurement with fixed bias voltage polarization of the sample was approximately 1 hour. Core level spectra were recorded once a steady current density was reached under the fixed bias voltage (except with the relatively unstable current at +5 V), as reported in the electronic supplementary Information (ESI), p. S-6, Figure S10 for T_150 and in ESI, p. S-6, Figure S11 for T_200.

As a reference data, Au 4f core level spectra from T_150 and T_200 are reported in the ESI, p. S-6, Figure S12. Spectra were acquired using different bias voltages applied to the bottom p^+-Si. As expected for the grounded Au layer, there is no significant binding energy difference (energy shift) when the applied bias voltage was modified. We also note that the Au 4f peak intensities and shapes remained identical during all *operando* analyses. The Au $4f_{7/2}$ binding energy of 84.0 eV was consistent with metallic gold (Au^0)[43]. The overall data analyses of core level spectra were performed with CasaXPS software[46] with a Shirley algorithm used to subtract the background and a pseudo-Voigt peak shape (Gaussian/Lorentzian with 30 % Lorentzian character) for the major peak fittings.

III. RESULTS AND DISCUSSION

A. Influence of the In_2O_3 deposition and PTA temperatures on the oxygen transfer process in the $In_2O_3/Al_2O_3/p^+$-Si stack

After the survey scans reported on ESI, p. S-2, Figure S1, the In 3d, Al 1s, O 1s core levels and the valence band HAXPES spectra of the T_150-bare and T_200-bare samples were recorded and shown in Figure 2 (a)-(d), respectively. The components and corresponding binding energies obtained by the peak fitting for each core level are listed in Table I. From Figure 2 (a), the In 3d deconvolution yielded three contributions attributable to different chemical states. Based on the report of Qi et al.[47], we attributed that the green (444.8

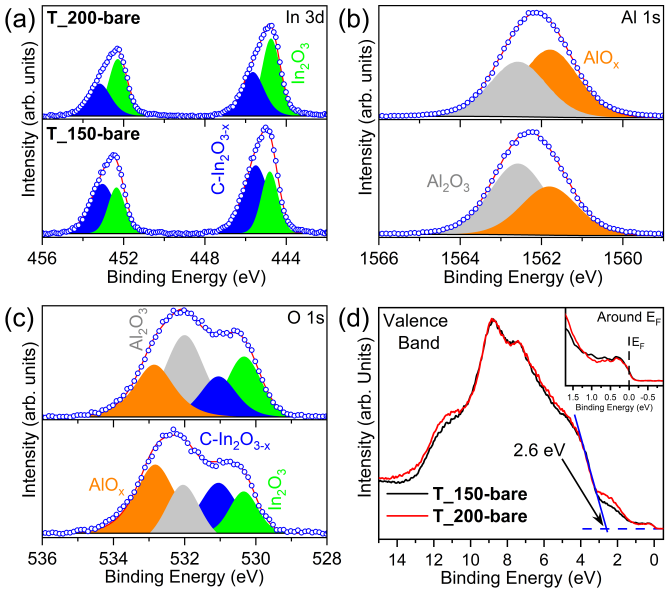

FIG. 2: Core level HAXPES spectra of T_150-bare and T_200-bare: (a) In 3d, (b) Al 1 s, and (c) O 1s binding energies and (d) the valence band spectra for T_150-bare and T_200-bare.

TABLE I: Summary of the fitting parameters used for the In $3d_{5/2}$, Al 1s, O 1s and Ti $2p_{3/2}$ peaks: the colours, components and binding energies in eV are listed.

Elements	Colors	Components	Binding energy (eV)
In $3d_{5/2}$	Red	In^0 (In-Ti)	443.3
	Green	In_2O_3	444.8
	Blue	C-In_2O_{3-x}	445.4
Al 1s	Orange	AlO_x	1561.8
	Gray	Al_2O_3	1562.5
O 1s	Green	In_2O_3	530.3 - 530.4
	Blue	C-In_2O_{3-x}	531.1
	Gray	Al_2O_3	532.0
	Orange	AlO_x	532.9
Ti $2p_{3/2}$	Cyan	Ti^0 - TiC	453.9 - 454.2
	Magenta	TiO	455.3
	Yellow	Ti_2O_3	457.4
	Olive	TiO_2	459.1

eV) and blue (445.4 eV) peaks were related to stochiomet-ric In_2O_3[48–50] and carbon-doped In_2O_3 (C-In_2O_{3-x}), respectively. From a combination of surface-sensitive X-ray photoelectron spectroscopy (XPS, $h\nu$ = 1.486 keV) experimental data and density functional theory (DFT) calculations, Qi et al. explained that the In 3d moved to a higher binding energy compared to that for In_2O_3.

From the peak fitting result shown in Figure 2 (a), we see that the C-In_2O_{3-x} signal for T_150-bare is larger than for T_200-bare. We observed the presence of the C-In_2O_{3-x} compound not only in T_150-bare but also in T_200-bare, contrary to what had been previously reported in some research[26]. We ascribed this contradiction to the fact that XPS used in[26] reports is surface-sensitive, while in this current work, bulk-sensitive HAXPES was used. In other words, we may assume that in the case of the T_200-bare sample, we have a gradi-ent in the carbon content from the surface of the In_2O_{3-x} film to the buried interface (In_2O_{3-x}/Al_2O_{3-x}). We associated this relatively high concentration of the blue peak with incomplete pyrolysis and dihydroxylation when the ALD growth temperature decreased. Thus, the variations in the C-In_2O_{3-x} sig-nal indicated that the C doping level may be tuned during the ALD process. Furthermore, from AFM (ESI, p. S-2, Figure S2) a decrease in the root mean square (RMS) surface roughness value from 0.73 and 0.16 nm is observed for T_150-bare and T_200-bare, respectively.

The Al 1s core level spectra in Figure 2 (b) indicate the presence of stoichiometric Al_2O_3 indicated by the grey peaks and oxygen-deficient Al_2O_3 (AlO_x) indicated by the orange peaks at 1562.5 eV and 1561.8 eV, respectively[51]. This indexation of components is consistent with the depth probing from the naked Al_2O_3 (-bare) reported in ESI, p. S-3, Figure S.3. By decreasing the information from 85^o (deep probing) to 10^o (shallow probing), we see the presence of contribution at lower binding energy from both Al 1s (ESI, p. S-3, Fig-ure S.3 (a)) and Al 2p (ESI, p. S-3, Figure S.3 (b)). We do not consider surface potential formation at the naked surface because the VBM (not shown here) of Al_2O_3 was found below Fermi energy (E_F)[52]. From ESI, p. S-3, Figure S.3 (c), we assume a mixed-valence state of Al, such as the coexis-tence of stoichiometric Al_2O_3 and non-stoichiometric Al_2O_3 (AlO_x) due to a lack of oxygen species (presence of $V_O{}^{2+}$). Then, from Figure 2 (b), we also highlight that the relative amount of AlO_x increased from the T_150-bare to the T_200-bare samples. As reported by Qi et al.[47], it is challenging to distinguish the $V_O{}^{2+}$-poor In_2O_3, $V_O{}^{2+}$-rich In_2O_{3-x} however, by increasing the temperature of In_2O_3 deposition, more $V_O{}^{2+}$ inside the In_2O_3 layer is likely generated. This result is also consistent with the fact a lack of oxygen in In_2O_3 will trigger an oxygen transport from Al_2O_3 to In_2O_3 and therefore we observe more AlO_x in T_200-bare than T_150-bare.

The O 1s peaks in Figure 2 (c) were deconvoluted into four components representing four different states associated to the Al_2O_3 and In_2O_3 layers. The green peak at approximately 530.3 - 530.4 eV was attributed to the oxygen in stochiometric In_2O_3[53]. Then the blue peak at 531.1 eV is associated with the C-In_2O_{3-x}[53]. The gray peak at 532.0 eV was assigned to the oxygen in stochiometric Al_2O_3[54] and the orange peak centered at 532.9 eV was from the AlO_x[54] due to the presence of $V_O{}^{2+}$.

Complementary depth profiling analyses along the T_200-bare stacked structure were carried out by changing TOA from 85^o (deep probing) to 20^o (shallow probing). While the In 3d energy position (not shown here) was not affected by TOA,

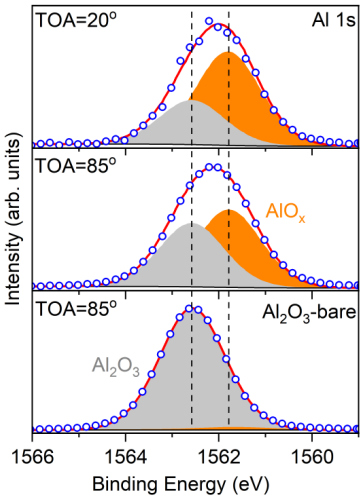

FIG. 3: Depth-dependent analyses: HAXPES spectra for the Al 1s state of Al_2O_3-bare at TOA of 85^o and T_200-bare samples at TOAs of 20 and 85^o.

the Al 1s position seemed to differ slightly with a TOA of 20^o as shown in Figure 3. In contrast to Al_2O_3-bare (Al_2O_3/p^+-Si), the T_200-bare results indicated the presence of substan-tial AlO_x contribution when using a similar TOA of 85^o. The AlO_x ratio was more important around the In_2O_3/Al_2O_3 inter-face as indicated by the TOA of 20^o. We attribute this oxy-gen gradient to a redistribution of oxygen between In_2O_3 and Al_2O_3 to mitigate the chemical potential mismatch as previously observed in the case of for TiO_2/VO_2.[56]. Indeed, a difference in oxygen chemical potential between two materials may give rise to oxygen ion transfer to bring the system into equilibrium. In this scenario, In_2O_{3-x} took oxygen from stochiometric Al_2O_3 to produce $V_O{}^{2+}$-like defects in the AlO_x. Mobile oxygen species were transferred to adjacent materials until the chemical potentials of the layers matched.

Furthermore, when comparing the AlO_x amount between the two samples in Figure 2 (c), we observe that the ALD growth temperature enhanced the oxygen transport. The relative quantification show an increase of AlO_x amount from $\sim$ 40% to $\sim$ 55% for T_150-bare and T_200-bare, respectively. This oxygen loss from Al_2O_3 layer by diffusion will reduced the $V_O{}^{2+}$ amount in the In_2O_3 layer. Bayer et al. observed similar phenomena during the deposition of Al_2O_3 on an ITO substrate[57]. They showed that the oxygen from the ITO substrate was the source of the additional reactant during the deposition of the Al_2O_3 layer. They assumed that the large growth per cycle observed during ALD process of the Al_2O_3 layer on the ITO substrate was only possible if an additional oxygen reactant was present for the formation of Al_2O_3. In the Bayer report, oxygen species were released at the surface and reacted with the trimethylaluminium (TMA) precursor to form Al_2O_3. The authors also reported that a sufficient concentration of interstitial oxygen was liberated from the ITO substrate to provide enough oxygen for the growth of a 1-2 nm Al_2O_3 layer. Finally, we add that although the oxygen species were sufficiently mobile at 200 °C[58], oxygen release was also observed at room temperature during the deposition of organic molecules onto clean ITO[59]. Based on the above discussion, we expected an identical process for our stacked $In_2O_3/Al_2O_3/p^+$-Si.

In Figure 4, we sketched models to explain the reduction process of the Al_2O_3 layer during the growth of In_2O_3. Fig-ure 4 (a) describes the first stage of the interaction between the Al_2O_3-bare and the InEtCp precursor. After completion of the first cycle of In_2O_3 growth, as shown in Figure 4 (b), $V_O{}^{2+}$ was present at the surface and in the bulk In_2O_3 layer. Now, because the In atoms from the InEtCp precursor specifically bond to oxygen at the surface upon exposure to the InEtCp precursor, a decrease in the In_2O_3 growth rate was observed. To partially compensate for this lack of oxygen, the diffusion of oxygen atoms from the Al_2O_3 substrate takes place, as illustrated by the red arrows in Figure 4 (b). This oxygen migra-tion process led to the creation of new $V_O{}^{2+}$ inside the Al_2O_3, as shown in Figure 4 (c).

From 150 °C to 200 °C, more significant oxygen transport occurred in Figure 4 (e) than in Figure 4 (d). At 200 °C, more oxygen atoms are extracted from the Al_2O_3 layer. As described theoretically with the DFT calculations[60], the oxygen atoms easily moved inside the In_2O_3 reached the surface and reacted with the InEtCp precursor to form a new In_2O_3 layer. This explanation is consistent with the higher AlO_x amount for T_200-bare compared to that for T_150-bare, as shown in Figure 2(b).

Finally, the effect of PTA on the T_150-bare and T_200-bare samples was also studied. Results from In 3d and Al 1s core levels before and after the PTA process are reported in the ESI, p. S-3, Figure S4. For both samples, no significant changes were observed for the normalized In 3d level after the PTA step. However, one noticed a slight re-oxidation of the covered Al_2O_3 layer after PTA. The stochiometric Al_2O_3 signal increased while that for the AlO_x material decreased. From the decrease of AlO_x, we argue that during the PTA process, oxygen species went through the In_2O_3 layer and partially compensated for the lack of oxygen in the Al_2O_3 layer.

As a summary of the ALD growth temperature and PTA effects, it is clear that oxygen transport process into the $In_2O_3/Al_2O_3/p^+$-Si stack may have sharply affected the de-vice performance. We observe that the ALD growth temper-ature for In_2O_3 controlled both the C-doping level and the $V_O{}^{2+}$ contents of the In_2O_3 and Al_2O_3 layers. We confirmed that the PTA process lowered the $V_O{}^{2+}$ sites inside the stacked In_2O_3/Al_2O_3 structure.

B. Impact of the patterned Au/Ti electrodes on the $Au/Ti/In_2O_3/Al_2O_3/p^+$-Si stack

The impact of Ti metal from Au/Ti electrode on In_2O_3 with a PTA process was studied. Chemical analysis of Ti/In_2O_3 interfaces from the T_150 and T_200 samples are shown in Figure 5. From the In 3d/Ti 2p core level spectra, we discern the oxidation states of titanium from Ti^0 to Ti^{2+} (magenta), Ti^{3+} (yellow), and Ti^{4+} (olive)[61,62]. Additionally, a small red component at 443.3 eV, indicative of the reduc-

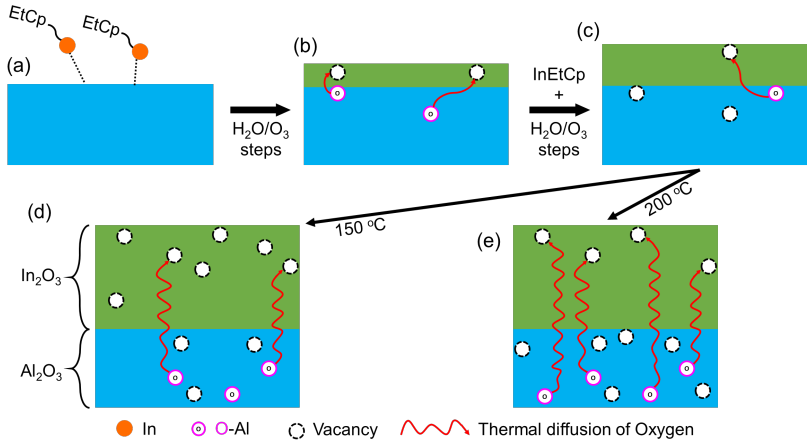

FIG. 4: Illustration of the oxygen migration driven by diffusion on In_2O_3/Al_2O_3 stack obtained by ALD. (a) Formation of the interface with the first layer of In_2O_3 on Al_2O_3-bare. (b) Oxygen migration from the Al_2O_3 substrate towards the interface with the fully developed initial layer of In_2O_3. (c) Emergence of oxygen vacancies within the Al_2O_3 layer showing the intricate interplay between the two materials. (d-e) Comparison of oxygen vacancies ratio within the Al_2O_3 layer resulting from In_2O_3 deposition at 150 °C and 200 °C respectively.

tion of indium with the In^0 component, was attributed to the metallic contribution of indium In^0 from the binary Ti-In system[63]. The binary Ti-In system is characterized by the mixture of indium and titanium at the Ti/In_2O_3 in-terface. Notably, the binding energy of In^0 (443.3 eV) ob-served in Figure 5 is lower than the expected binding en-ergy of pure indium (443.8 eV) from a reference source, as reported in the ESI, p. S-4, Figure S5 (c). This devia-tion towards the negative direction (decreased binding en-ergy) of In^0 can be attributed to changes in the electronic structure, bonding interactions, or chemical environment surrounding the indium atoms within the Ti-In alloy. The binding energies and the corresponding components are re-ported in Table I. Regarding the In_2O_3 reduction process, a complementary depth profiling analysis was initially carried out on the T_200 reference sample (with as-deposited In_2O_3 and without PTA). First, results revealed that In^0 species were mainly located at the Ti/In_2O_3 interface. As seen in the ESI, p. S-4, Figure S6 (a) and (b), we observe a reduction of In_2O_3 (Green arrow) relative to In^0 (red arrow) when the TOA goes down (from deep or bulk to shallow or interfacial probing). This result is consistent with the reduction of stochiometric In_2O_3 and an increase of In^0 around the Ti/In_2O_3 junction. Then, for the partial oxidation of Ti, the results also indicated that the Ti oxidation process was triggered by Ti deposition and did not require any PTA. Indeed, based on the reactivity of Ti and its strong affinity for oxygen, the Ti layer should take up oxygen from the In_2O_3 layer. In addition, oxygen transport towards the Ti layer may be facilitated by the relatively weak In-O bond in the case of In_2O_3 structure. In fact, with a un-stable Ti/In_2O_3 interface, oxygen atoms could preferentially migrate from In_2O_3 to form the more stable TiO_2 interlayer. To determine which tie-line is theoretically favored at room temperature deposition (25 °C), the two possible tie-line reactions are written in the form of balanced chemical reactions:

$$Ti(s) + 2In_2O_3(s) = 4In(s) + 3TiO_2(s);$$
$$\Delta G^o_{rxn} = 3G^o_{TiO_2} - 2G^o_{In_2O_3} \sim -988.5; (T = 25^oC)$$

From the standard 25 °C thermodynamic values, the standard Gibbs free energy (ΔG^o_{rxn}) was found by summing the formation energies of the oxides multiplied by their stoichiometry metric coefficients. Since ΔG^o_{rxn} was negative, the forward reaction was favoured, and we conclude that the stable tie-line for this system connected In metal to TiO_2 and that the Ti in contact with In_2O_3 formed an unstable interface. Finally, we add that the TOA analysis of Al 1s from ESI, p. S-4, Figure S6 (c) does not support the existence of dropping electrostatic potential (gradient) across the Al_2O_3 layer after the deposition and partial oxidation of Ti top layer on In_2O_3 layer. This explanation is consistent with the fact regardless of the angle of measurement the Al 1s remain unchanged (identical shape and position). No shift or change relative to a band bending.

As for the PTA impact, we have observed an important oxidation of Ti to TiO_2 with PTA as reported in Figure 5. For both T_150 and T_200 samples, the total amount of Ti^0 was more than halved by the PTA, which led to the creation of a thick ($\geq$ 2.5 nm) titanium oxide intermediate layer (as supported by the ESI, p. S-5, Figure S7). We assumed that the In_2O_3 acted as an oxygen tank during PTA and then released some of the stored oxygen into the Ti layer. We also expect that the significant amount of TiO_2 will increase the $V_O{}^{2+}$ concentra-tion in the In_2O_3 layer. This gradual increase in $V_O{}^{2+}$ would then provoke a second oxygen migration (compensation pro-cess), which would take place between the In_2O_3 and Al_2O_3 layers. A shift towards a lower Al 1s binding energy with in-creasing titanium oxide concentration was confirmed (green curve in ESI, p. S-5, Figure S8). This energy shift was asso-ciated with an increase in the amount of AlO_x remaining after oxygen species left the Al_2O_3 layer.

Moreover, we underline that the binding energies of Ti metal in Figure 5 is slightly shifted towards the higher energy relative to the Ti^0 position when In_2O_3 underwent a PTA pro-cess, as seen in Figure 5. The Ti^0 peak at 453.9 eV exhibited a BE shift of 0.3 eV towards higher energy due to the presence of titanium carbide (454.2 eV[64]). The presence of carbon on the Ti layer also suggested residual carbon transport from the In_2O_3 layer to the Ti film during the PTA (a heat treatment performed below 150 °C). We note that, unlike the wide band gap for TiO_2, which is not a good electrical conductor, TiC is a good electrical conductor[65,66] and can likely play a central role in determining the channel-to-source (or drain) interface resistivity in case of actual TFT.

In light of these results, we can expect that the oxygen deficiency at the In_2O_3/TiO_2 junction as well as the presence of TiC will act as a highly doped n^+ contact (n^+ channel/source (drain) region in the case of an actual TFT device). The V_O^{2+} will serve as an electron source that forms a semiconductor and leads to a low-resistivity interface. With the existence of the upper n^+ contact side, the region of In_2O_3 near the Al_2O_3 layer can be considered the less conductive surface (doped n^-). Therefore, In_2O_3-TFT with a Ti electrode may have an n^-n^+/metal junction in the source (drain) region, leading to better ohmic behavior.

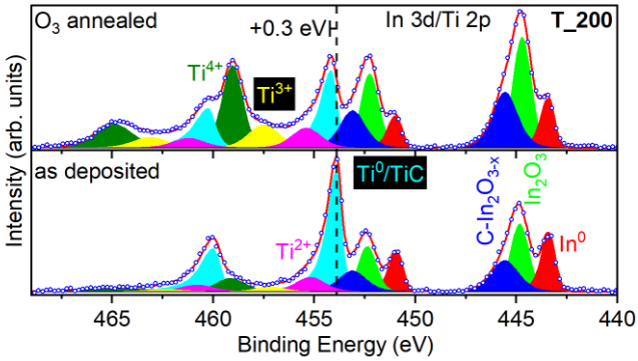

FIG. 5: In 3d/Ti 2p core levels for T_200 ($Au/Ti/In_2O_3/Al_2O_3/p^+$-Si structure) with and without the PTA process under an O_3 atmosphere for the $In_2O_3/Al_2O_3/p^+$-Si stack (T_200-bare).

C. Chemical analysis of the $Au/Ti/In_2O_3/Al_2O_3/p^+$-Si structure under an applied bias voltage

Operando-HAXPES analysis was carried out under an applied bias voltage to investigate the electric field effects on T_150 and T_200 samples. Before the *operando* analysis, a standard current-voltage measurement was performed on samples as reported in the ESI, p. S-5, Figure S9.

Figure 6 illustrates the binding energies and peak shapes of Al 1s and Si 2p for (Figure 6 (a-b)) and T_200 (Figure 6 (c-d)) stacked devices. Similar trends in energy shifts were observed for both samples. Regarding Si 2p (Figure 6 (b)-(d)), it is noted that, except for the -1 V bias voltage setting, the effective or actual applied bias voltage across the devices tends to be lower than the set values (1V, 5V). Specifically, the Si 2p shift is notably lower than the applied voltage when +1V or 5V are applied. Under normal circumstances, the Si 2p positions are expected to shift concerning the Si 2p 0V_forward reference by almost the exact applied voltage amount, particularly for heavily doped p^+-Si substrates. This approximation holds for a voltage of -1V. However, for +5 V applied on T_150 and T_200 samples, the Si 2p from p^+-Si substrates experi-ences a shift ranging from +1.7 eV to +2.0 eV, respectively. These findings suggest limited penetration of the electric field into the heavily doped p-type Si. Notably, the effec-tive bias voltage applied to heavily doped p-type Si may deviate from the set bias voltage due to various factors, including contact potential, depletion region, series resistance, external circuit impedance, etc. Therefore, the ex-act cause of this lower effective bias voltage on the stacked devices cannot be definitively determined. However, issues related to the complex outer HAXPES circuit connection or current flow have been ruled out, as evidenced by the nearly -1 eV Si 2p shift observed at -1 V. Furthermore, de-spite the lower effective bias voltage compared to the ap-plied voltage, the impact of the bias voltage on Al_2O_3 and In_2O_3 functional layers, the main focus of this study, was successfully demonstrated. Lastly, no significant broaden-ing of the Si 2p peak was observed with applied voltage, with the full width at half maximum (FWHM) of the Si 2p3/2 remaining between 0.39 eV and 0.46 eV.

Chemical alterations occurring on the Al_2O_3 layers in response to applied bias voltages on the p^+-Si substrate are also elucidated in Figure 6 (a)-(c). It is crucial to emphasize that due to the time-consuming nature of the analysis, we only utilized a single take-off angle (TOA) to record chemical changes. Consequently, it becomes challenging to discern binding energy shifts associated with variations in the built-in potential gradient and intensity changes based on depth analysis. The impact of the built-in potential on the spectrum with this single TOA can only be anticipated through the asymmetric broadening of core levels. In both samples, an asymmetrical energy shift along the energy axis relative to the 0 V curve, as well as band bending induced by the electrostatic poten-tial across the stacked devices, were observed. Notably, the presence of a global energy shift of the symmetric spectral shape along the energy axis led us to dismiss the possibility of potential chemical changes under an applied bias volt-age. Additionally, it is noteworthy that the Al 1s shifts are lower than the Si 2p core levels when the same bias volt-age is applied. This suggests that the electrostatic potential drop within the Al_2O_3 layer and the broadening of the Al 1s peak at +5 V are more likely induced by band bend-ing and/or an interfacial effect between Al_2O_3 and p^+-Si (interface energy barrier).

Figure 7 reports In 3d/Ti 2p core level spectra from T_150 and T_200 samples. For both samples, analyses were car-ried out with similar bias stresses (0V_forward, +1V, +5V, 0V_reverse, and -1V). As expected after PTA of the In_2O_3 layer and the deposition of Ti, a significant TiO_2 contribution, as well as a Ti^0 shift due to the additional TiC signal, was observed. We also note that for both samples, variations in the applied bias voltages did not affect the chemistry of the Ti layer. This result was consistent with the fact that the Au/Ti was grounded.

In Figure 7, we observe that the residual binding energy shift of the In $3d_{5/2}$ peak around 445 eV (red dot line) is associated with the In_2O_3 growth temperature but not to the bias voltages applied to the samples. This In $3d_{5/2}$ shift is related to the difference of In_2O_3 and C-In_2O_{3-x} amount between samples, as presented in Figure 2 (a). Furthermore, under applied a progressive bias voltage, no significant modification (shape and intensity) was detected for the T_200 sample, in

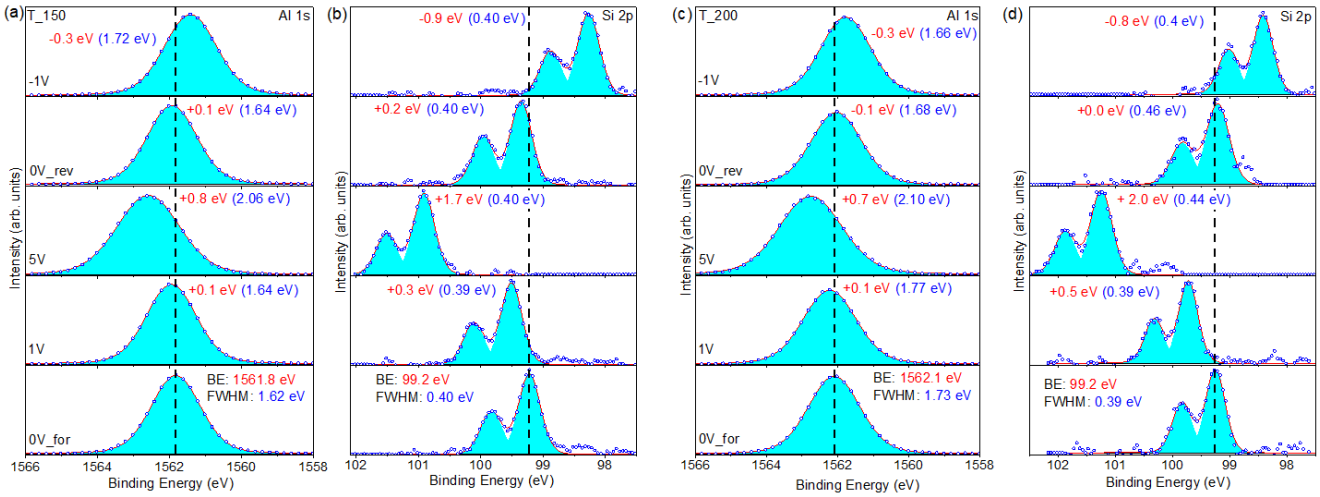

FIG. 6: Core level spectra from Al 1s in (a)-(c) and Si 2p in (b)-(d) from T_150 and T_200 samples, respectively under an applied bias voltage (0 V_forward, 1 V, 5 V, 0 V_reverse and -1 V. We note that the Al 1s and Si 2p core level spectra from T_150 and T_200 displayed the same trends for the binding energy (in red) shifts and full width at half maximum (fwhm in blue) under the applied voltage.

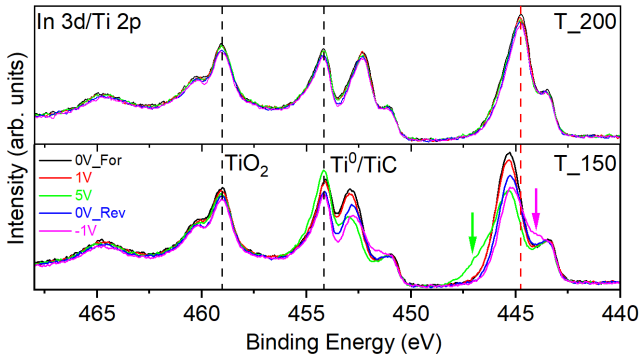

FIG. 7: In 3d/Ti 2p core level as a function of the externally applied voltage bias (0V_forward, 1V, 5V, 0V_reverse, and -1V).

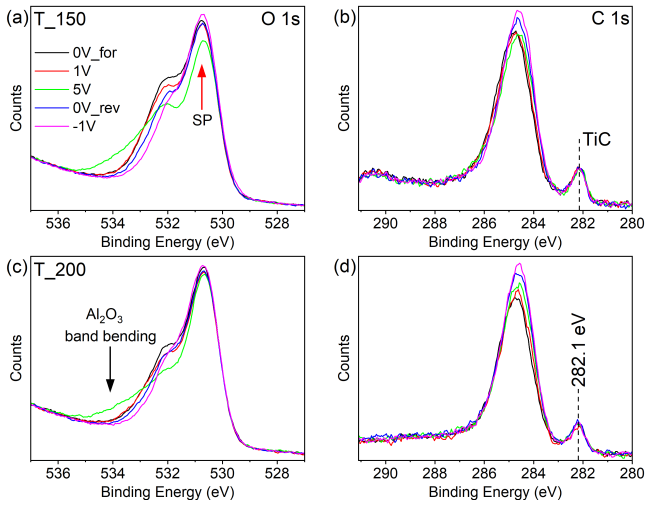

FIG. 8: O 1s and C 1s core levels determined for T_150 (a-b) and T_200 (c-d) with *operando*-HAXPES analyses under an applied bias voltage (0V_forward, 1V, 5V, 0V_reverse and -1V).

contrast to the T_150 sample. As emphasized by the arrows, T_150 shows a voltage-dependent phase (denoted as a splitting phase (SP)) as well as clear variations in the maximum intensities at +5 V, 0_rev, and -1V, and contrarily 0_for and +1V.

Figure 8 provides additional evidence on the SP phase. As we have seen from Figure 2 (a)-(c), the two first components (green and blue) and the two last peaks (gray and orange) of O 1s core levels are consistent with the peak fitting of In 3d (In_2O_3) and Al 1s (Al_2O_3), respectively. This relationship leads to the fact that any chemical change observed from In 3d or Al 1s will likely induce a change in the O 1s curves. Therefore, similar to In 3d (Figure 7) and Al 1s (Figure 6), from O 1s core levels from Figure 8 (a) and (c), we noted that the shapes of O 1s peaks are also bias voltage-dependent. With the T_200 sample in Figure 8 (c), the change of O 1s shape starts from 532 eV. As highlighted by the black arrow, the presence of a significant tail out to 536 eV is observed in the case of +5 V. This feature induced by the band bending under the bias voltage was ascribed to Al_2O_3 as already discussed in the experimental section (B). Besides the Al_2O_3 band bending component, with the T_150 sample, an extra intensity variation of around 531 eV is also observed as indicated by the red arrow. This latter intensity variation is related to the indium oxide layer. This modification of O 1s intensity was tightly correlated with the emergence of the SP phase and was more visible at +5 V. We note that a certain threshold bias voltage was needed to generate the splitting phase for both the In 3d and O 1s core levels from In_2O_3.

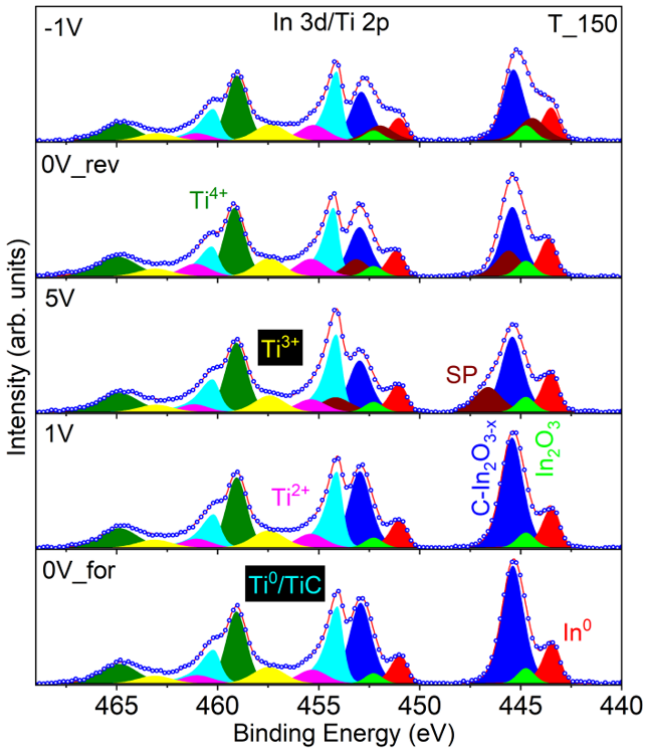

FIG. 9: Deconvolution of the In 3d and Ti 2p core levels as a function of the bias voltage (0V_forward, 1 V, 5 V, 0 V_reverse and -1 V) applied on the T_150 sample during the *operando*-HAXPES analyses. For 5 V, 0 V_reverse, and -1 V, the In 3d level showed a supplementary component ascribed to splitting (SP for splitting phase) of C-In_2O_{3-x} (blue) under the bias stress. The chemical state of the Ti 2p contribution (Ti^0/TiC, TiO, Ti_2O_3, and TiO_2) was unaffected over the voltage range with a major contribution from the TiO_2 olive peak.

From C 1s data in Figure 8 (b) and Figure 8 (d), we do not observe a direct link between the carbon species and the SP phase observed for the T_150 sample under a bias voltage. However, the presence of TiC interlayer associated with the C 1s component at 282.1 eV was confirmed in both samples. This TiC is induced by the migration of carbon species into the Ti layer.

In Figure 9, In 3d/Ti 2p curve fitting of T_150 sample as the function of the applied bias voltage is reported. The SP signal (wine peak) began to distinctly appear with a +5 V bias voltage and was induced by the splitting of C-In_2O_{3-x} component shown in blue in Figure 9. Relative to the C-In_2O_{3-x} peak at 445.4 eV, the binding energy shifts of the SP under the +5 V, 0_rev, and -1 V bias voltages are +1.2 eV, +0.1 eV, and -1.0 eV, respectively. We also note that the SP shift followed the same trends as the Si 2p and Al 1s core levels as reported in Figure 6. Since the Au/Ti was grounded, we argue that chemical splitting took place at the In_2O_3/Al_2O_3 interface and was triggered by interfacial band bending of the In_2O_3 layer. In addition, we did not observe an energy shift from the TiO_x contributions. For the T_200 sample, peak fitting data are reported in ESI, p. S-7, Figure S13.

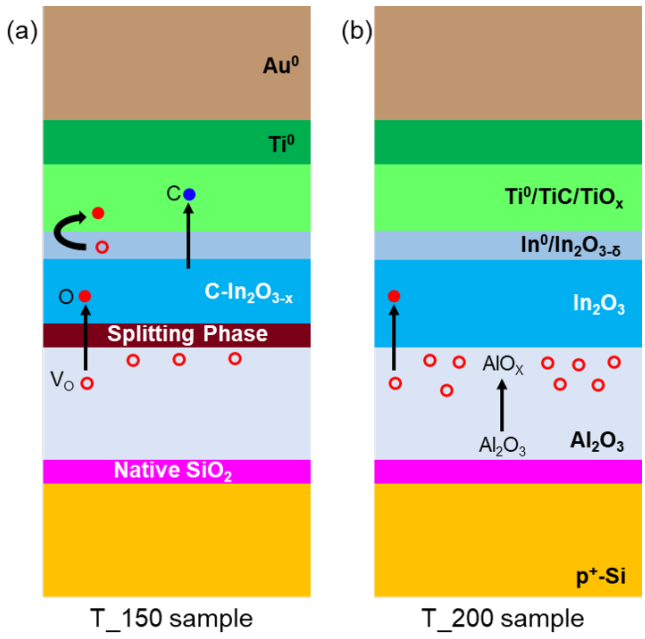

FIG. 10: Schematic cross-sectional view of the Au/Ti/In_2O_3/Al_2O_3/SiO_x/p^+-Si stacked structure deposited at: (a) T_150 and (b) T_200 samples. The arrows indicate the directions for oxygen and carbon movement.

With a penetration of the electric field into the In_2O_3 film, the appearance of the SP for T_150 upon voltage application can have various origins such as the interaction of the electrical field with the chemical impurities, defects, charge accumu-lation/depletion, and even interfacial chemical reactions. The presence of this splitting phase also suggests that the T_150 sample (higher C-In_2O_3 contribution) is much more resistive than the T_200 sample (lower C-In_2O_3 contribution). This decrease of conductivity of T_150 is consistent with the fact the presence of doping carbon (C-In_2O_3) reduces the excess of oxygen vacancies (by raising the oxygen bond dissociation energy and reducing the excess of electrons from the remain-ing oxygen vacancies), and decreases the very high and un-controlled n-type conduction. As splitting occurred at the in-terface under a certain threshold voltage, we cannot exclude a self-forming interfacial dipole[67–70] or interfacial electrochem-ical polarization mechanism in the present study. This in-terfacial state could be associated with the steep shift of the band structure across the interfaces. Indeed, with the In_2O_3 semiconductor-like T_150 sample, the charge carriers at the In_2O_3/Al_2O_3 interface are not suppressed by the injection or release of electrons from the grounded Ti/Au electrodes. Thus, the presence of an increased charge potential due to the interfacial charge might result in the polarization of the bottom side of the In_2O_3 layer and then lead to the formation of a separation phase for T_150.

In Figure 10, we graphically summarized the chemical models for T_150 and T_200 stacked structures after the bias voltage was applied. In this model, we intentionally included

the native SiO_2 interlayer as already discussed in our previous paper[43]. For both samples, the presence of AlO_x near the In_2O_3/Al_2O_3 interface resulted from oxygen diffusion into the indium oxide layer and compensated for the oxygen deficiency. Based on peak fitting of the In 3d core levels, the indium oxide layers from T_150 and T_200 are labelled as C-In_2O_{3-x} and In_2O_3, respectively. The presence of reactive Ti metal at the indium oxide surface led to a substantial oxy-gen shortage in the indium oxide layer. Ti removed oxygen and carbon species from the indium oxide film and then scavenged them for the Ti layer. These transported species led to the creation of interfacial $In^0/In_2O_{3-\delta}$ on the side of the indium oxide top interface and intermediate TiC/TiO_x (TiO, Ti_2O_3, TiO_2) on the Ti bottom edge. In response to the bias voltage applied at the p^+-Si substrate, both samples exhibited band bending along the Al_2O_3 layer. Furthermore, no additional chemical change occurred at the Ti (TiC and TiO_x) adhesion layer under electrical polarization. Within this model, we highlight that in contrast to the metal-like T_200 sample, the incorporation of carbon into the In_2O_3 matrix increased the semiconductor-like behavior (T_150), which formed a splitting phase at the In_2O_3/Al_2O_3 interface under the applied electric field. This splitting phase undergoes a band bending which follows a similar direction to that of the Al_2O_3 layer.

By qualitatively analyzing the HAXPES data, we observe that the ALD growth temperature and the post-annealing strongly affect the In_2O_3 film and its adjacent layers. We hypothesize that the imprint towards the negative bias as reported in ESI, p. S-5, Figure S9 can be linked to the interfacial defects (presence of energy barrier) while the hysteresis can be related to the back-and-forth movement of ionic species across layers.

IV. CONCLUSIONS

In this paper, we performed a non-destructive chemical analysis of an Au/Ti/In_2O_3/Al_2O_3/p^+-Si stacked structure. The study casts light on the impact of the ALD growth temperature and the post-annealing treatment as well. HAXPES analysis revealed that the chemical composition of the In_2O_3 semiconductor was temperature dependent, and the deposition of In_2O_3 on the Al_2O_3 insulator layer triggered oxygen transport from the insulator to the semiconductor to counterbalance the intrinsic oxygen deficiency of In_2O_3.

With the Au/Ti patterned samples, we observed the migration of the oxygen and carbon species from the In_2O_3 layer to the Ti layer. This C and O absorption generated TiO_2 and TiC interlayers. Using *operando*-HAXPES analyses under applied voltages, Al_2O_3 band bending leading to charge accumulation at the In_2O_3/Al_2O_3 interface was observed. Conversely to the In_2O_3 metal-like in T_200 sample, we observe a presence of the splitting phase in the In_2O_3 semiconductor-like behavior in T_150 sample. We argue that this splitting phase in T_150 sample was induced by the position-dependent charge carriers around the In_2O_3/Al_2O_3 interface. From this paper, we note that the ALD growth temperature as well as the post-annealing treatment impacts may have major repercussions for interpreting and optimizing actual TFT performance as suggested by the analysis of the Au/Ti/In_2O_3/Al_2O_3/p^+-Si stacked devices.

SUPPORTING INFORMATION

HAXPES spectra of wide range survey scans of Stacked Au/Ti/In_2O_3/Al_2O_3/p^+-Si; Surface morphologies of the T_150-bare and T_200-bare samples; HAXPES depth profile analysis of naked-Al_2O_3; In $3d_{5/2}$ and Al 1s core levels from T_150-bare and T_200-bare samples; Al 1s binding energy shifts for T_200 as a function of annealing under O_3; HAXPES depth profiling analyses of the Au/Ti/In_2O_3/Al_2O_3/p^+-Si without PTA on In_2O_3/Al_2O_3/p^+-Si; In 3d/Ti 2p core levels from stacked T_150 and T_200 with and without PTA; Current density-voltage (J-V) characteristic; Investigation of the stability of the T_150 sample over time; Investigation of the stability of the T_200 sample over time; Au 4f, Al 1s and Si 2p core level spectra for T_150 and T_200 samples under an applied bias voltage; Deconvolution of the In 3d and Ti 2p core level spectra as a function of the applied bias voltage.

NOTES

The authors declare no competing financial interest.

ACKNOWLEDGEMENTS

This work was partially supported by JSPS KAKENHI (Grant No: 20H02188). The HAXPES measurements were performed under the approval of the NIMS Synchrotron X-ray Station (Proposal No. 2020A4602 and 2020A4651).

[1] Anthopoulos,T. D.; Noh, Y.-Y.; Jurchescu, O. D. Emerging Thin-Film Transistor Technologies and Applications, Adv. Funct. Mater. 2020, 30, 2001678, https://doi.org/10.1002/adfm.202001678

[2] Paterson, A. F. Anthopoulos, T. D. Enabling thin-film transistor technologies and the device metrics that matter, Nat Commun. 2018 9, 5264, https://doi.org/10.1038/s41467-018-07424-2

[3] Sheng, J., Han, K.-L.; Hong, T.; Choi, W.-H.; Park, J.-S. Review of recent progresses on flexible oxide semiconductor thin film transistors based on atomic layer deposition processes, J. Semicond. 39, 011008 (2018), https://doi.org/10.1088/1674-4926/39/1/011008

[4] Fortunato, E.; Barquinha, P.; Martins, R. Oxide semiconductor thin-film transistors: a review of recent advances, Adv. Mater. 24, 2945-2986 (2012),

https://doi.org/10.1002/adma.201103228

[5] Kamiya, T.; Hosono, H. Material characteristics and applications of transparent amorphous oxide semiconductors, NPG Asia Mater. 2010, 2(1) 15-22, https://doi.org/10.1038/asiamat.2010.5

[6] Park, J. W.; Kang, B. H.; Kim, H. J. A Review of Low-Temperature Solution-Processed Metal Oxide Thin-Film Transistors for Flexible Electronics, Adv. Funct. Mater. 2020, 30, 1904632, https://doi.org/10.1002/adfm.201904632

[7] Bierwagen, O. Indium oxide-a transparent, wide-band gap semiconductor for (opto)electronic applications, Semicond. Sci. Technol. 30 (2015) 024001, https://doi.org/10.1088/0268-1242/30/2/024001

[8] Aikawa, S.; Nabatame, T.; Tsukagoshi, K. Effects of dopants in InO_x-based amorphous oxide semiconductors for thin-film transistor applications, Appl. Phys. Lett. 103, 172105 (2013), https://doi.org/10.1063/1.4822175

[9] Walsh, A.; Da Silva, J. L. F .; Wei, S.-H.; Körber, C.; Klein, A.; Piper, L. F. J.; DeMasi, A.; Smith, K. E. Panaccione, G.; Torelli, P.; Payne, D. J.; Bourlange, A.; Egdell, R. G. Nature of the Band Gap of In_2O_3 Revealed by First-Principles Calculations and X-Ray Spectroscopy, PRL 100, 167402 (2008), https://doi.org/10.1103/PhysRevLett.100.167402

[10] Karazhanov, S. Zh.; Ravindran, P.; Vajeeston, P.; Ulyashin, A.; Finstad, T. G.; Fjellvåg, H. Phase stability, electronic structure, and optical properties of indium oxide polytypes. Physical Review B, 76(7), 075129 (2007) https://doi:10.1103/physrevb.76.075129

[11] Irmscher, K.; Naumann, M.; Pietsch, M.; Galazka, Z.; Uecker, R.; Schulz, T.; Schewski, R.; Albrecht, M.; Fornari, R. On the nature and temperature dependence of the fundamental band gap of In ₂ O ₃. physica status solidi (a), 211(1), 54-58 (2014). https://doi:10.1002/pssa.201330184

[12] Muydinov, R.; Steigert, A.; Wollgarten, M.; Michaowski, P.; Bloeck, U.; Pflug, A.; Erfurt, D.; Klenk, R.; Körner, S.; Lauermann, I.; Szyszka, B. Crystallisation Phenomena of In2O3:H Films. Materials, 12(2), 266 (2019) https://doi:10.3390/ma12020266

[13] Kim, H.Y.; Jung, E.A.; Mun, G.; Agbenyeke, R.E.; Park, J.S.; Son, S.U.; Jeon, D.J.; Park, S. H. K.; Chung, T.M.; Han, J.H. Low-temperature growth of indium oxide thin film by plasma enhanced atomic layer deposition using liquid dimethyl(N-ethoxy-2,2-dimethylpropanamido)indium for high-mobility thin film transistor application, ACS Appl. Mater. Interfaces 8 (40) (2016) 26924-26931, https://doi.org/10.1021/acsami.6b07332

[14] Fuh, C.-S.; Liu, P.-T.; Chou, Y.-T.; Teng L.-F.; Sze S. M. Role of Oxygen in Amorphous In-Ga-Zn-O Thin Film Transistor for Ambient Stability, ECS J. Solid State Sci. Technol. 2, Q1 (2013). https://doi.org/10.1149/2.012301jss

[15] Aikawa, S.; Nabatame, T.; Tsukagoshi, K. Si-incorporated amorphous indium oxide thin-film transistors, Jpn. J. Appl. Phys. 58 090506 (2019). https://doi.org/10.7567/1347-4065/ab2b79

[16] Kurishima, K.; Nabatame, T.; Kizu, T.; Mitoma, N.; Tsukagoshi, K.; Sawada, T.; Ohi, A.; Yamamoto, I.; Ohishi, T.; Chikyow, T.; Ogura, A. Prospectively of carbon-doped indium-tungsten-oxide channel TFT for bias stress instability. ECS Trans. 75, 149-156 (2016), https://doi.org/10.1149/07510.0149ecst

[17] Strand, J.; Shluger, A. L. On the Structure of Oxygen Deficient Amorphous Oxide Films, Adv. Sci. 2024, 11, 2306243, https://doi.org/10.1002/advs.202306243

[18] Buchholz, D. Bruce; Ma, Qing; Alducin, Diego; Ponce, Arturo; Jose-Yacaman, Miguel; Khanal, Rabi; Medvedeva, Julia E.; Chang, Robert P. H. (2014). The Structure and Properties of Amorphous Indium Oxide. Chemistry of Materials, 26(18), 5401-5411. doi:10.1021/cm502689x

[19] Liu, L.; He, C. C.; Zeng, J.; Peng, Y. H.; Chen, W. Y.; Zhao, Y. J.; Yang, X. B. Theoretical Study of Oxygen-Vacancy Distribution in In_2O_3, J. Phys. Chem. C 2021, 125, 13, 7077-7085, https://doi.org/10.1021/acs.jpcc.1c01462

[20] Tiwari, N.; Nirmal, A.; Kulkarni, M.R.; John, R.A.; Mathews, N. Enabling high performance n-type metal oxide semiconductors at low temperatures for thin film transistors, Inorg. Chem. Front., 2020, 7, 1822-1844, https://doi.org/10.1039/d0qi00038h

[21] Reunchan, P.; Zhou, X.; Limpijumnong, S.; Janotti, A.; Van de Walle, C. G. Vacancy defects in indium oxide: An ab-initio study, Curr. Appl Phys. 11, S296-S300 (2011), https://doi.org/10.1016/j.cap.2011.03.051

[22] Kim, T.; Jang, B.; Lee, S.; Lee, W.; Jang, J. Improved Negative Bias Stress Stability of Sol-Gel-Processed Mg-Doped In2O3 Thin Film Transistors, IEEE Electron Device Letters, 2018 39, 12, 1872-1875, https://doi.org/10.1109/LED.2018.2873622.

[23] Flewitt, A. J.; Powell, M. J. A thermalization energy analysis of the threshold voltage shift in amorphous indium gallium zinc oxide thin film transistors under simultaneous negative gate bias and illumination, J. Appl. Phys. 2014, 115, 134501, https://doi.org/10.1063/1.4870457

[24] Wang, W.; He, G.; Yu, H.; Gao, Q.; Wang, L.; Xu, X.; Zhang, Y.; Wu, X.; He, B. Enhanced electrical performance and stability of La-doped indium oxide-based thin-film transistors and application explorations. Phys. Status Solidi A (2021), 219, 2100590, https://doi.org/10.1002/pssa.202100590

[25] Lee, S. H.; Kim, T.; Lee, J.; Avis, C.; Jang, J. Solution-processed gadolinium doped indium-oxide thin-film transistors with oxide passivation, Appl. Phys. Lett. (2017), 110, 122102, https://doi.org/10.1063/1.4978932

[26] Kobayashi, R.; Nabatame, T.; Onaya, T.; Ohi, A.; Ikeda, N.; Nagata, T.; Tsukagoshi, K.; Ogura, A. Comparison of characteristics of thin-film transistor with In_2O_3 and carbon-doped In_2O_3 channels by atomic layer deposition and post-metallization annealing in O_3, Jpn. J. Appl. Phys. 60 030903 (2021), https://doi.org/10.35848/1347-4065/abde54

[27] Tang, T.; Dacha, P.; Haase, K.; Kreß, J.; Hänisch, C.; Perez, J.; Krupskaya, Y.; Tahn, A.; Pohl, D.; Schneider, S.; Talnack, F.; Hambsch, M.; Reineke, S.; Vaynzof, Y.; Mannsfeld, S. C. B. Analysis of the Annealing Budget of Metal Oxide Thin-Film Transistors Prepared by an Aqueous Blade-Coating Process, Adv. Funct. Mater.2023, 33, 2207966, https://doi.org/10.1002/adfm.202207966

[28] Ma, Q.; Zheng, H. M.; Shao, Y.; Zhu, B.; Liu, W. J.; Ding, S. J.; Zhang, D. W. Atomic-Layer-Deposition of Indium Oxide Nano-films for Thin-Film Transistors, Nanoscale Res. Lett. 13, 4 (2018), https://doi.org/10.1186/s11671-017-2414-0

[29] Yeom, H. I.; Ko, J. B.; Mun, G.; Park, S. H. High mobility polycrystalline indium oxide thin-film transistors by means of plasma-enhanced atomic layer deposition, J. Mater. Chem. C, 2016, 4, 6873-6880, https://doi.org/10.1039/C6TC00580B

[30] Nomura, K.; Kamiya, T.; Ohta, H.; Hirano, M.; Hosono, H. Defect passivation and homogenization of amorphous oxide thin-film transistor by wet O_2 annealing. Appl. Phys. Lett. 93, 192107 (2008), https://doi.org/10.1063/1.3020714

[31] Lee, S.; Bierig, B.; Paine, D.C. Amorphous structure and electrical performance of low-temperature annealed amorphous indium zinc oxide transparent thin

film transistors. Thin Solid Films 520, 3764 (2012), https://doi.org/10.1016/j.tsf.2011.06.082

[32] Nomura, K.; Kamiya, T.; Hirano, M.; Hosono, H. Origins of threshold voltage shifts in room-temperature deposited and annealed α-InGaZnO thin-film transistors, Appl. Phys. Lett. 95, 013502 (2009), https://doi.org/10.1063/1.3159831

[33] Lim, W. T.; Norton, D. P.; Jang, J. H.; Craciun, V.; Pearton, S. J.; Ren, F. Carrier concentration dependence of Ti/Au specific contact resistance on *n*-type amorphous indium zinc oxide thin films, Appl. Phys. Lett. 92, 122102 (2008), https://doi.org/10.1063/1.2902322

[34] Shimura, Y.; Nomura, K.; Yanagi, H.; Kamiya, T.; Hirano, M.; Hosono, H. Specific contact resistances between amorphous oxide semiconductor In-Ga-Zn-O and metallic electrodes, Thin Solid Films 516, 5899 (2008), https://doi.org/10.1016/j.tsf.2007.10.051

[35] Lee, S.; Park, H.; Paine, D.C. A study of the specific contact resistance and channel resistivity of amorphous IZO thin film transistors with IZO source-drain metallization, J. Appl. Phys. 109, 063702 (2011), https://doi.org/10.1063/1.3549810

[36] Kwon, J.-Y.; Lee, D.-J.; Kim, K.-B. Transparent amorphous oxide semiconductor thin film transistor, Electron. Mater. Lett. 7, 1 (2011), https://doi.org/10.1007/s13391-011-0301-x

[37] Nag, M.; Bhoolokam, A;. Steudel, S.; Genoe, J.; Groeseneken, G.; Heremans, P. Impact of the low temperature gate dielectrics on device performance and bias-stress stabilities of a-IGZO thin-film transistors, ECS J. Solid State Sci. Technol. 4 (8) N99-N102 (2015), https://doi.org/10.1149/2.0121508jss

[38] Yim, J.-R.; Jung, S.-Y.; Yeon, H.-W.; Kwon, J.-Y.; Lee, Y.-J.; Lee, J.-H.; Joo, Y.-C. Effects of Metal Electrode on the Electrical Performance of Amorphous InGaZnO Thin Film Transistor, Jpn. J. Appl. Phys. 51 011401 (2011), https://doi.org/10.1143/JJAP.51.011401

[39] Gueye, I.; Le Rhun, G.; Renault, O.; Cooper, D.; Defay, E.; Barrett, N. Correlation of electrical characteristics with interface chemistry and structure in Pt/Ru/$PbZr_{0.52}Ti_{0.48}O_3$/Pt capacitors after post metallization annealing, Appl. Phys. Lett. 113, 132901 (2018); https://doi.org/10.1063/1.5041767

[40] Gueye, I.; Le Rhun, G.; Renault, O.; Cooper, D.; Ceolin, D.; Rueff, J.-P.; Barrett, N.; Operando hard X-ray photoelectron spectroscopy study of the Pt/Ru/$PbZr_{0.52}Ti_{0.48}O_3$ interface, Appl. Phys. Lett. 111, 032906 (2017); https://doi.org/10.1063/1.4993909

[41] Woicik, J. C. Hard X-ray Photoelectron Spectroscopy (HAXPES) (Springer Ser. Surface Sc, Springer, Berlin, 2016), https://doi.org/10.1007/978-3-319-24043-5

[42] Mizutani, F.; Higashi, S.; Inoue, M.; Nabatame, T. Atomic layer deposition of stoichiometric In_2O_3 films using liquid ethylcyclopentadienyl indium and combinations of H_2O and O_2 plasma, AIP Advances 9, 045019 (2019), https://doi.org/10.1063/1.5081727

[43] Gueye, I.; Kobayashia, R.; Ueda, S.; Nabatame, T.; Tsukagoshi, K.; Ogura, A.; Nagata, T. Operando hard X-ray photoelectron spectroscopy study of buried interface chemistry of Au/$In_{1.16}O_{0.04}$/Al_2O_3/p^+-Si stacks, Applied Surface Science 593 (2022) 153272, https://doi.org/10.1016/j.apsusc.2022.153272

[44] Ueda, S.; Katsuya, Y.; Tanaka, M.; Yoshikawa, H.; Yamashita, Y.; Ishimaru, S.; Matsushita, Y.;Kobayashi, K. Present Status of the NIMS Contract Beamline BL15XU at Spring-8, AIP Conf. Proc. 1234, 403-406 (2010), https://doi.org/10.1063/1.3463225

[45] Tanuma, S.; Powell, C. J.; Penn, D. R. Calculations of electron inelastic mean free paths. V. Data for 14 organic compounds over the 502000 eV range, Surf. Interface Anal. 1994, 21, 165-176, https://doi.org/10.1002/sia.740210302

[46] Walton, J.; Wincott, P.; Fairley, N.; Carrick, A. Peak Fitting with CasaXPS: A Casa Pocket Book. Knutsford, UK: Accolyte Science, 2010

[47] Qi, Y.; Jiang, J.; Liang, X.; Ouyang, S.; Mi, W.; Ning, S. Zhao, L.; Ye, J. Fabrication of Black In_2O_3 with Dense Oxygen Vacancy through Dual Functional Carbon Doping for Enhancing Photothermal CO_2 Hydrogenation, Adv. Funct. Mater.2021, 31, 2100908, https://doi.org/10.1002/adfm.202100908

[48] Kim, S.; Carpenter, P. D.; Jean, R. K.; Chen, H.; Zhou, C.; Ju, S.; Janes, D. B. Role of Self-Assembled Monolayer Passivation in Electrical Transport Properties and Flicker Noise of Nanowire Transistors, ACS Nano. 2012, 6, 8, 7352-7361, https://doi.org/10.1021/nn302484c

[49] Henegar, A. J.; Gougousi, T. Native oxide transport and removal during the atomic layer deposition of Ta_2O_5 on InAs(100) surfaces, J. Vac. Sci. Technol. A 2016, 34, 031101, https://doi.org/10.1116/1.4945115

[50] Kyndiah,A.; Ablat, A.; Guyot-Reeb, S.; Schultz, T.; Zu, F.; Koch, N.; Amsalem, P.; Chiodini, S.; Alic, T. Y.; Topal, Y.; Kus, M.; Hirsch, L.; Fasquel, S.; Abbas, M. Multifunctional Interlayer for Solution Processed High Performance Indium Oxide Transistors. Sci Rep. 2018, 8, 10946, https://doi.org/10.1038/s41598-018-29220-0

[51] Mendes, M. K.; Martinez, E.; Marty, A.; Veillerot, M.; Yamashita, Y.; Gassilloud, R.; Bernard, M.; Renault, O.; Barrett, N. Forming mechanism of Te-based conductive-bridge memories. Appl. Surf. Sci. (2018) 432, 34-40, https://doi.org/10.1016/j.apsusc.2017.07.187

[52] Ohashi, N.; Yoshikawa, H.; Yamashita, Y.; Ueda, S.; Li, J;. Okushi, H.; Kobayashi, K.; Haneda, H. Determination of Schottky barrier profile at Pt/SrTiO3:Nb junction by x-ray photoemission, Appl. Phys. Lett. 101, 251911 (2012) https://doi.org/10.1063/1.4772628

[53] Nayak, P. K.; Hedhili, M. N.; Cha, D.; Alshareef, H. N. High performance In_2O_3 thin film transistors using chemically derived aluminum oxide dielectric, Appl. Phys. Lett. 103, 033518 (2013), https://doi.org/10.1063/1.4816060

[54] Liu, Q.; Qin, H.; Boscoboinik, J. A.; Zhou, G. Comparative Study of the Oxidation of NiAl(100) by Molecular Oxygen and Water Vapor Using Ambient-Pressure Xray Photoelectron Spectroscopy, Langmuir, 2016, 32, 11414, https://doi.org/10.1021/acs.langmuir.6b02752

[55] Ma, H. P.; Yang, J. H.; Yang, J. G.; Zhu, L. Y.; Huang, W.; Yuan, G. J.; Feng, J. J.; Jen, T. C.; Lu, H. L. Systematic Study of the SiO_x Film with Different Stoichiometry by Plasma-Enhanced Atomic Layer Deposition and Its Application in SiO_x/SiO_2 Super-Lattice, Nanomaterials, 2019, 9, 55, https://doi.org/10.3390/nano9010055

[56] Park, Y.; Sim, H.; Jo, M.; Kim, G.-Y.; Yoon, D.; Han, H.; Kim, Y.; Song, K.; Lee, D.; Choi, S.-Y.; Son, J. Directional ionic transport across the oxide interface enables low-temperature epitaxy of rutile TiO_2. Nat Commun 11, 1401 (2020). https://doi.org/10.1038/s41467-020-15142-x

[57] Bayer, T. J. M.; Wachau, A.; Fuchs, A.; Deuermeier, J.; Klein, A. Atomic Layer Deposition of Al_2O_3 onto Sn-Doped In_2O_3: Absence of Self-Limited Adsorption during Initial Growth by Oxygen Diffusion from the Substrate and Band Offset Modification by Fermi Level Pinning in Al_2O_3, Chem. Mater. 2012, 24, 23, 4503-4510, https://doi.org/10.1021/cm301732t

[58] Quaas, M.; Steffen, H.; Hippler, R.; Wulff, H. Investigation of diffusion and crystallization processes in thin ITO films by temperature and time resolved grazing incidence X-ray diffractometry, Surface Science 540 (2003) 337-342,

https://doi.org/10.1016/S0039-6028(03)00850-1

[59] Lee, K. H.; Jang, H. W.; Kim, K.-B.; Tak, Y.-H.; Lee, J.-L. Mechanism for the increase of indium-tin-oxide work function by O_2 inductively coupled plasma treatment, J. Appl. Phys. 95, 586 (2004); https://doi.org/10.1063/1.1633351

[60] Ágoston,P.; Albe, K. Ab initio modeling of diffusion in indium oxide, Phys. Rev. B (2010) 81, 195205, http://dx.doi.org/10.1103/PhysRevB.81.195205

[61] Shvab, R.; Hryha, E.; Nyborg, L. Surface chemistry of the titanium powder studied by XPS using internal standard reference, Appl. Surf. Sci., 2014, 295, 180-188, https://doi.org/10.1080/00325899.2016.1271092

[62] Biesinger, M. C.; Lau, L. W. M.; Gerson, A. R.; Smart, R. S. C. Resolving surface chemical states in XPS analysis of first row transition metals, oxides and hydroxides: Sc, Ti, V, Cu and Zn, Appl. Surface Sci., 2010 257, 887-898, https://doi.org/10.1016/j.apsusc.2010.07.086

[63] Gulay, L. D.; Schuster, J. C. Investigation of the titanium-indium system. J. Alloy. Compd. 360, 137-142 (2003) https://doi.org/10.1016/S0925-8388(03)00319-0.

[64] Park, J.; Back, T.; Mitchel, W. C.; Kim, S. S.; Elhamri, S.; Boeckl, J.; Fairchild, S. B.; Naik, R.; Voevodin, A. A. Approach to multifunctional device platform with epitaxial graphene on transition metal oxide. Sci Rep. 2015, 5, 14374, https://doi.org/10.1038/srep14374

[65] Yukun, P.; Hua, X.; Rasit, K. Investigation of Electrical Conductivity and Oxidation Behavior of TiC and TiN Based Cermets for SOFC Interconnect Application, ECS Transactions, 7 (1) 2427-2435 (2007), https://doi.org/10.1149/1.2729365

[66] Guo, Q.; Wu, T.; Liu, L.; Hou, H.; Chen, S.; Wang, L. Flexible and conductive titanium carbidecarbon nanofibers for the simultaneous determination of ascorbic acid, dopamine and uric acid, J. Mater. Chem. B, 2018,6, 4610-4617, https://doi.org/10.1039/C8TB00938D

[67] Schaefer, M.; Halpegamage, S.; Batzill, M.; Schlaf, R. Investigation of the dipole formation and growth behavior at $In_2O_3|TiO_2$ heterojunctions using photoemission spectroscopy and atomic force microscopy, J. Appl. Phys. 119, 065305 (2016); https://doi.org/10.1063/1.4940954

[68] Lang, O.; Pettenkofer, C.; Sanchez-Royo J. F.; Segura, A.; Kleina, A.; Jaegermann, W. Thin film growth and band lineup of In_2O_3 on the layered semiconductor InSe, J. Appl. Phys. 86, 5687 (1999); https://doi.org/10.1063/1.371579

[69] Chen, Q.; Wang, C.; Li, Y.; Chen, L.; Interfacial Dipole in Organic and Perovskite Solar Cells, J. Am. Chem. Soc. 2020, 142, 43, 18281-18292, https://doi.org/10.1021/jacs.0c07439

[70] Chokawa, K.; Shiraishi, K. Self-forming and self-decomposing gallium oxide layers at the GaN/Al2O3 interfaces, Applied Physics Express 12, 061008 (2019), https://doi.org/10.7567/1882-0786/ab21b4